UC Santa Barbara

UC Santa Barbara Previously Published Works

Title

Evolution of noncollinear magnetism in magnetocaloric MnPtGa

Permalink

https://escholarship.org/uc/item/4x88093q

Journal

Phys. Rev. Mater., 4(4)

Author

Seshadri, Ram

Publication Date

2020-04-13

DOI

10.1103/PhysRevMaterials.4.044405

Peer reviewed

eScholarship.org Powered by the California Digital Library
University of California

Evolution of non-collinear magnetism in magnetocaloric MnPtGa

Joya A. Cooley,[1,*] Joshua D. Bocarsly,[1,2] Emily C. Schueller,[1,2] Emily E. Levin,[1,2]
Efrain E. Rodriguez,[3] Ashfia Huq,[4] Saul H. Lapidus,[5] Stephen D. Wilson,[2] and Ram Seshadri[1,2,6]

[1]*Materials Research Laboratory, University of California, Santa Barbara, 93106*
[2]*Materials Department, University of California, Santa Barbara, 93106*
[3]*Department of Chemistry and Biochemistry, University of Maryland, College Park, Maryland 20742*
[4]*Neutron Scattering Division, Oak Ridge National Laboratory, Oak Ridge, Tennessee 37831*
[5]*X-ray Sciences Division, Argonne National Laboratory, Lemont, Illinois 60439*
[6]*Department of Chemistry and Biochemistry, University of California, Santa Barbara, 93106*

MnPtGa crystallizes in the hexagonal Ni_2In structure type in space group $P6_3/mmc$, and has been reported to display a ferromagnetic Curie temperature near 220 K. Here we find a transition near T_C = 236 K to a ferromagnetic state, albeit with a reduced moment from what is expected for collinear ordering. The peak magnetocaloric entropy change was determined to be $\Delta S_M = -1.9\,\mathrm{J\,kg^{-1}\,K^{-1}}$ for an applied magnetic field of $H = 5$ T at the ferromagnetic ordering temperature. Magnetostructural coupling manifests as a change in the slope of the thermal expansion coefficients of the c lattice parameter near T_C, with a negative spontaneous volume magnetostriction; $\omega = -300$ ppm at 190 K. Neutron powder diffraction studies of the magnetic ground state reveal an evolution in complexity as temperature decreases: from a ferromagnet, to a canted antiferromagnet, to the eventual formation of a spin-density wave state at low temperatures.

INTRODUCTION

Magnetic materials containing 5d transition elements are often found to have a richness of observed properties. In addition to the potential for magnetic hardening associated with the strong spin-orbit coupling effects of the later 5d elements [1, 2], these compounds can display invar effects [3, 4], complex magnetostructural behavior [5] and the potential for hosting magnetic Weyl fermions [6]. In this regard, we have closely investigated MnPtGa which is a thus-far not very well studied compound in the Ni_2In structure type, first described by Buschow *et al.* in 1983 [7]. The compound is reported to be ferromagnetic near 220 K and to crystallize in the hexagonal Ni_2In structure type in space group $P6_3/mmc$. Furthermore, this material has recently been suggested as possessing a broken center of inversion symmetry, allowing which allows it to display thermodynamically stable Neél-type skyrmions between around 210 K and 220 K, and metastable skyrmions in a much broader temperature range down to at least 5 K [8].

It has been suggested that promising candidate materials for magnetic refrigeration *via* the magnetocaloric effect can be evaluated through a computational proxy known as magnetic deformation, or Σ_M [9, 10]. This proxy is a predictor of the strength of magnetostructural coupling in a given material calculated using density functional theory (DFT). When DFT-based structural optimizations are performed with and without spin polarization, the difference between the two relaxed structures can be quantified as Σ_M, in which a high value is found to correspond with a strong magnetocaloric effect. The calculated Σ_M can be correlated with magnetocaloric properties even in materials where the magnetic transition is not coupled to a structural phase transition [11]. Through this proxy, MnPtGa emerged as a candidate meriting experimental study for high magnetocaloric performance. Magnetic deformation calculations of MnPtGa showed Σ_M = 2.4%, and prior findings have classified Σ_M greater than 1.5% as promising.

Upon preparing and studying MnPtGa, however, we found that its magnetic properties, including its magnetization *vs.* temperature, saturated moment, and magnetocaloric effect were inconsistent with those of a simple collinear ferromagnet, as it has been reported to be. This motivated us to used neutron powder diffraction and DFT to understand the evolution of the magnetic structure below T_C.

Here we present a detailed structural and magnetic characterization of MnPtGa using magnetic measurements, synchrotron and neutron powder diffraction, and density functional theory calculations. Our samples adopt a hexagonal Ni_2In-type nuclear structure and exhibit a complex temperature evolution of magnetic structure, including ferromagnetic and canted antiferromagnetic phases and a canted spin-density wave ground state. Temperature-dependent synchrotron diffraction reveals that these magnetic phase transitions are coupled magnetoelastically to the lattice parameters. These rich magnetic states are also expected to impact the formation and behavior of skyrmions and other long-wavelength chiral magnetic states.

I. MATERIALS AND METHODS

Polycrystalline ingots of MnPtGa were prepared using a combination of arc-melting and furnace annealing. Elemental Mn (99.95%, Alfa Aesar) was cleaned before use by annealing overnight sealed in an evacuated fused

* jacooley@mrl.ucsb.edu

silica tube at 1273 K. Purified Mn was then ground and combined with Pt powder (99.9%, Strem) and pieces of Ga buttons (Alfa Aesar, 99.9999%) totaling about 0.5 g (or 1.5 g, for neutron diffraction samples). 10 atomic % excess Mn was added to account for Mn loss during heating. Pre-weighed Mn and Pt powders were pelletized into 6 mm pellets, then arc-melted with Ga in an Ar atmosphere, turned over, and melted again for homogeneity. The resultant ingot was wrapped in Ta foil, sealed in an evacuated fused silica ampoule (approx. 8 cm length, 9.5 mm ID) and annealed for 6 days at 1073 K. The furnace was turned off and allowed to cool to room temperature.

Neutron powder diffraction data were collected at 300 K, 200 K, 150 K, 50 K and 10 K at the POWGEN diffractometer [12] at the Spallation Neutron Source at Oak Ridge National Laboratory on 1.5 g of polycrystalline powder. Patterns at all temperatures were collected using a center wavelength of the neutron packet of 2.665 Å, and additional patterns using a center wavelength of 0.8 Å were collected at 300 K and 10 K. The longer wavelength data provides extremely high resolution and sensitivity at low Q, while the shorter wavelength data provides a much larger Q range. The magnetic structure supercells were determined with the aid of the K-Search program included with FullProf Suite [13] and the magnetic structures were solved with the aide of ISODISTORT [14, 15] and TOPAS Academic V6 [16]. Representations of the nuclear and magnetic structures were drawn with VESTA-3 [17]. Atomic displacement parameters (B_{eq}) were determined at 300 K and 10 K from co-refinement of data from center wavelengths 2.665 Å and 0.8 Å. For the intermediate temperatures, only center wavelength 2.665 Å data were available and therefore B_{eq} values were fixed to values linearly interpolated between the 300 K and 10 K data to reduce correlations.

Temperature-dependent synchrotron powder X-ray diffraction (XRD) data were collected using the area detector on beamline 11-BM at the Advanced Photon Source (APS), Argonne National Laboratory ($\lambda \approx 0.4$ Å). Due to the high X-ray absorption of Pt at this wavelength, the powder was adhered to the outside of a 1.1 mm ID Kapton capillary with a small amount of vacuum grease. The sample was cooled from 280 K to 180 K using a nitrogen cryostream at a rate of 0.4 K min^{-1}. 10 minute scans were taken resulting in each scan averaging over 4 K using $\lambda = 0.412825$ Å. For further analysis, additional measurements were taken with a 2-D area detector in which the sample was cooled from 300 K to 100 K at rate of 5 K min^{-1} using a nitrogen cryostream. During the cooling, a diffraction image was taken every 20 sec using $\lambda = 0.457845$ Å). The 2-D images were integrated using GSAS-II [18], and the patterns were refined sequentially using TOPAS Academic V6.

The possibility of compositional inhomogeneity in MnPtGa was examined using an FEI Apreo C scanning electron microscope (SEM). A piece from the arc melted ingot was mounted in epoxy and ground using SiC paper, and then polished down to 0.25 μm using diamond suspension. Images were acquired at an accelerating voltage of 5 keV using a backscattered electron (BSE) detector, which provides both electron density contrast and orientation contrast. For composition analysis, sample powder was blended with ≈10 weight % SPEX 3646 Paraffin Binder, pelletized into a 6 mm disk, and 5 points across the pellet surface were analyzed by a Rigaku ZSX Primus VI wavelength dispersive X-ray fluorescence (XRF) instrument using a 0.5 mm spot size.

Magnetic properties were measured on 6 mg to 10 mg of powder ground from an annealed ingot in a Quantum Design MPMS3 equipped with a vibrating sample magnetometer (VSM). For zero field cooled and field cooled measurements, magnetization (M) *vs.* temperature (T) data were acquired upon warming at a rate of 7 K min^{-1}. An Arrott plot was constructed with one quadrant M *vs.* applied field (H) measurements (*i.e.* 0 T to 5 T) at 3 K intervals between 170 K and 260 K. In order to determine ΔS_M, M *vs.* T measurements were taking on cooling at various fields from $H = 0.1$ T to $H = 5$ T. The temperature dependence of ΔS_M for a magnetic field change of 0 T to 5 T was derived from isothermal magnetization curves using the Maxwell relation:

$$\left(\frac{\partial S}{\partial H}\right)_T = \left(\frac{\partial M}{\partial T}\right)_H \tag{1}$$

which relates the slope of magnetization *vs.* temperature to the slope of entropy (S) *vs.* field. The field–driven isothermal entropy change ΔS_M can then be calculated using:

$$\Delta S_M(H,T) = \int_0^H \left(\frac{\partial M}{\partial T}\right)_{H'} dH' \tag{2}$$

Temperature derivatives of the $M(T)$ traces were calculated using Tikhonov regularization [19], and then integrals with field were calculated using the trapezoid method to obtain ΔS_M. This procedure was carried out using the `magentro.py` code [20].

Electronic structure calculations were performed using density functional theory, as implemented in the Vienna Ab initio Simulation Package (VASP) [21] with projector augmented wave (PAW) pseudopotentials [22, 23] within the Perdew-Burke-Ernzerhof (PBE) generalized gradient approximation (GGA) [24]. First, the hexagonal unit cell of MnPtGa was relaxed in non spin-polarized and spin-polarized calculations with a force convergence of 0.001 eV Å^{-1} and no spin-orbit coupling included. The spin-polarized calculation was then initialized with a starting ferromagnetic moment of 3 μ_B per Mn. Densities of states with and without spin-polarization were obtained from static calculations on these structures using a 10×10×8 Γ-centered k-point grid and an energy convergence criterion of 10^{-5} eV. Calculations including spin-orbit interactions were performed under the same con-

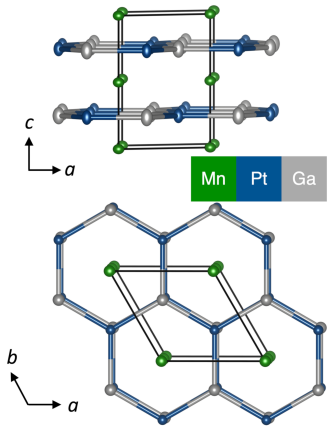

FIG. 1. Two views of the MnPtGa crystal structure are shown with with atoms represented using displacement ellipsoids shown at 95% probability. The structure is viewed down the b axis to emphasize how Pt-Ga layers alternate with Mn layers, and down the c axis to emphasize the honeycomb Pt-Ga lattice.

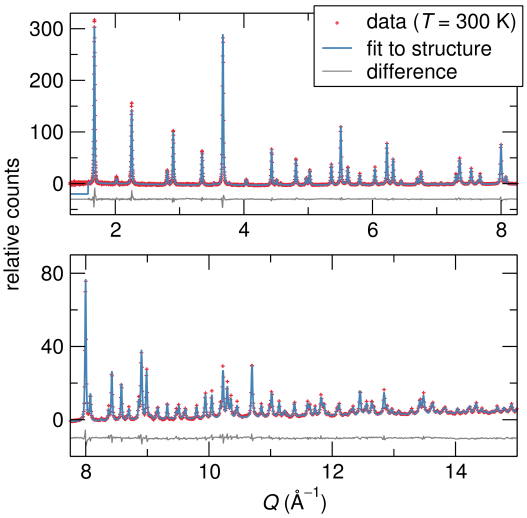

FIG. 2. Rietveld refinement results of the $T = 300$ K neutron powder diffraction data fit to the structure in the $P6_3/mmc$ space group, revealing a single phase sample fit with high certainty. For greater clarity, the fits are shown separately for lower and higher Q in the upper and lower panels. In both panels, the difference has been offset.

ditions, starting with collinear ferromagnetic spin structures with the spins either aligned in the [100] or [001] directions. In addition, a constrained moment calculation was performed to simulate the canted antiferromagnetic structure. In this calculation, an energy penalty was used to constrain the moments to angles of 22° from the [001] direction with no constraint on moment magnitudes.

II. RESULTS AND DISCUSSION

A. Structural characterization

MnPtGa has been previously reported to form in the hexagonal Ni_2In structure type (space group $P6_3/mmc$, No. 194) [25], as depicted in Fig. 1. The structure can be visualized as a honeycomb lattice of Pt and Ga atoms (in the $2c$ and $2d$ Wyckoff sites, respectively). These atoms are connected in the ab plane, and stacked along the c axis in alternating (*ABAB*) slabs offset in the ab plane by $\frac{1}{3}$ of the unit cell. The PtGa slabs are stuffed with Mn (site $2a$) ordered on a hexagonal lattice.

A recent report by Srivastava *et al.* [8] showed the formation of Néel-type skyrmions in a single-crystal sample of MnPtGa. The stabilization of magnetic skyrmions implies a crystal structure with a non-centrosymmetric space group, which is in agreement with their finding of the polar space group $P3m1$ (No. 156) for their crystals rather than the previously reported centrosymmetric $P6_3/mmc$ structure. The $P3m1$ structure differs from the $P6_3/mmc$ by a symmetry-breaking corrugation of the Pt-Ga honeycomb layers. Srivastava *et al.* present single-crystal X-ray diffraction data that clearly shows the presence of weak peaks which are forbidden by $P6_3/mmc$ extinction rules, but are allowed in $P3m1$, namely, $(00l)$ with $l = 2n + 1$. However, we see no evidence of these space group violations in our samples using synchrotron XRD and NPD at temperatures between 10 K and 300 K. Given the resolution and sensitivity of the diffraction instrumentation utilized in this work, we would expect to be able to easily resolve the weak peaks arising from the structure reported by Srivastava *et al.*, as demonstrated in Supplemental Material Figs. S1 and S2. Therefore, we conclude that differences in sample preparation for the powder samples in this study *vs.* the Bridgeman-grown single-crystal samples in the Srivastava *et al.* report evidently lead to slightly different crystal structures. However, we note that the Mn sublattice in both crystal structures is the same; therefore, we expect that similar magnetic structures to those we report for our samples are likely to form in samples with the distorted crystal structure. Further research is clearly called for in order to determine how subtle compositional and preparation details can be used to control the structural (and therefore skyrmionic) properties of MnPtGa.

Room-temperature neutron powder diffraction (NPD) data are shown in Fig. 2 along with a structural Rietveld refinement to the $P6_3/mmc$ structure-type. The fit to the data shows that the sample is single phase, with all observed peaks matching the model. The Pt site is found to contain approximately 1.50(4)% Mn, while the Mn and Ga sites are fully occupied with their respective atoms. Refined lattice parameters [$a = 4.3313(3)$ Å, $c = 5.5738(6)$ Å] are within 1% of both the room-temperature parameters provided by a previous report in $P6_3/mmc$ [25].

The large Q-space range of POWGEN data with center wavelength 0.8 Å (Fig. S4 of the Supplemental Material)

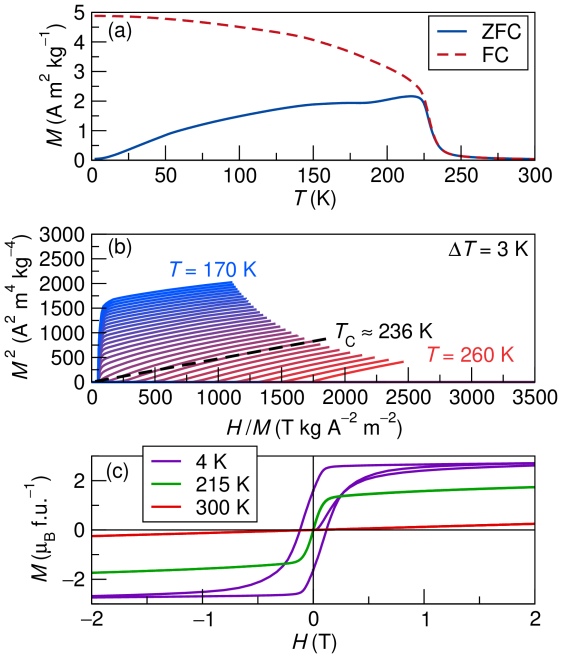

FIG. 3. (a) Temperature–dependent zero field-cooled (ZFC) and field-cooled (FC) magnetization measurements of MnPtGa measured under a $H = 20\,\text{mT}$ field reveal complex magnetic behavior with T_C near 230 K, and additional ordering near 200 K in the ZFC trace and near 150 K in the FC trace. (b) Isothermal field–dependent magnetization measurements are plotted in the Arrott style to emphasize the true T_C near 236 K. (c) Field–dependent magnetization measurements at 300 K, 215 K, and 4 K reveal that both M_{sat} and coercivity increase with decreasing temperature.

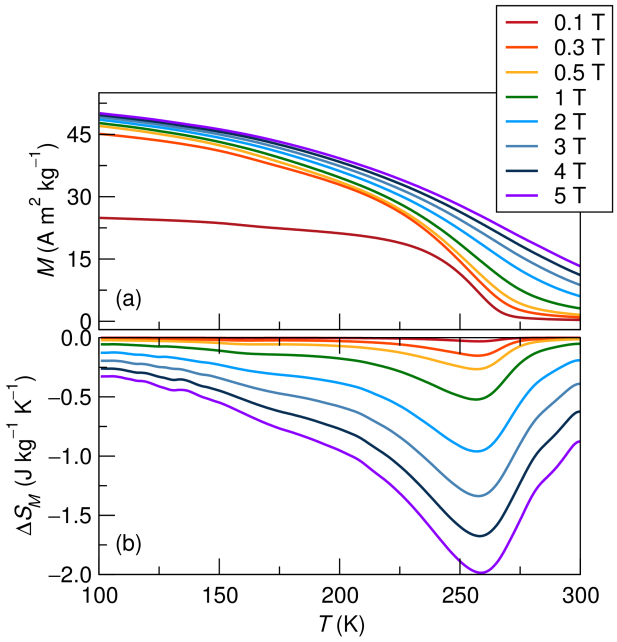

FIG. 4. (a) Temperature–dependent magnetization is measured at select fields to calculate ΔS_M. Derivatives of each curve are calculated and and integrated according to Equation 2, yielding ΔS_M shown in (b).

allows for the accurate refinement of anisotropic atomic displacement parameters (ADPs), which are shown as 95% ellipsoids in Fig. 1. While the Mn atom motion is relatively spherical, the Pt and Ga ADPs are much more anisotropic with more vibration occurring perpendicular to the basal plane at room temperature. As expected, the heavier Pt atoms have smaller displacements than the Ga atoms. The phase purity of the sample was further confirmed using backscattered electron microscopy (Fig. S3 of the Supplemental Material). XRF analysis revealed an average composition of $\text{Mn}_{1.067(3)}\text{Pt}_{0.978(3)}\text{Ga}_{0.956(5)}$, suggesting a slight excess of Mn. Further details of XRF analysis can be found in Table S1 of the Supplemental Material.

B. Magnetic property characterization

Figure 3(a) displays the temperature–dependent magnetization of MnPtGa between 2 K and 300 K under an applied field (H) of 20 mT. Both zero–field–cooled (ZFC) and field–cooled (FC) data are shown. Below the ordering temperature of approximately 230 K, clear thermomagnetic irreversibility is observed between the ZFC and FC measurements. In addition, kinks in the magnetization below the Curie temperature in the both the ZFC (near 200 K) and FC (near 150 K) curves can be seen, which suggests additional magnetic transitions below the Curie temperature.

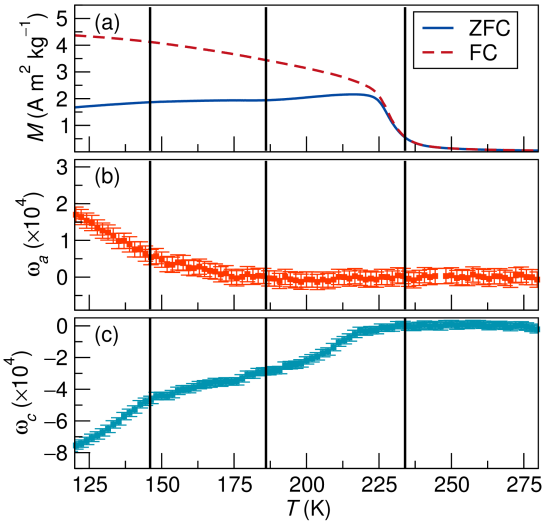

FIG. 5. (a) Temperature–dependent ZFC and FC magnetization measured under a $H = 20\,\text{mT}$ field are compared to (b) magnetostriction along the a axis, ω_a and (c) magnetostriction along the c axis, ω_c to emphasize structural changes coincident with magnetic phenomena.

Fig. 3(b) depicts M *vs.* H data plotted using the Arrott formalism [26] (*i.e.* M^2 *vs.* H/M) to determine the T_C of MnPtGa. The isothermal measurement which extrapo-

lates to the origin on this type of plot is taken as the T_C. The obtained T_C of 236 K agrees reasonably well with that reported by Buschow *et al.* [25] (220 K), especially considering the variability in different T_C determination techniques.

Fig. 3(c) shows representative $M(H)$ curves measured at several temperatures below T_C. The 300 K $M(H)$ is linear showing no additional ordering in this field range, and isotherms below the ordering temperature show ferromagnet-like magnetic saturation. Magnetic hysteresis is not seen at 215 K, but at 4 K an open hysteresis loop with a coercive field of $\mu_0 H_C = 120$ mT is observed. This magnetic hysteresis is consistent with the large low-temperature irreversibility seen between the zero-field cooled and field-cooled $M(T)$. The saturated moment increases as temperature is decreased, reaching a maximum $M_{sat} = 2.63\,\mu_B$ at 4 K and 1.8 T. This is somewhat smaller than the $M_{sat} = 3.15\,\mu_B$ found in a previous study [7], however it is significantly lower than DFT-calculated ferromagnetic moment of $3.58\,\mu_B$, a second indicator that there may be ordering beyond simple collinear ferromagnetism at low temperatures.

Fig. 4 shows a characterization of the magnetocaloric magnetic entropy change (ΔS_M) at different temperatures and fields. ΔS_M is the entropy change yielded by isothermal application of an external magnetic field, $\Delta S_M(H,T)$. The peak value of ΔS_M will occur near the Curie temperature where the magnetization changes quickly as a function of temperature, as seen in Equation 1. Figure 4(a) shows smoothed $M(T)$ data at several magnetic field strengths. These curves were differentiated with respect to temperature and integrated with respect to field, resulting in $\Delta S_M(T,H)$ shown in Fig. 4(b).

For a field change of $\Delta H = 5$ T the peak ΔS_M is –1.9 J kg^{-1} K^{-1}. This value is smaller than expected based on the Σ_M prediction. FeB, which has a similar Σ_M (2.2% for FeB *vs.* 2.4% MnPtGa), has a larger gravimetric peak ΔS_M of –3.2 J kg^{-1} K^{-1} [11]. Other materials in reference 9 with similar Σ_M have even larger ΔS_M. However, this analysis is affected by the presence of heavy Pt, which makes up 61% of MnPtGa by mass. The volumetric ΔS_M of MnPtGa is –22.3 mJ cm^{-3} K^{-1} (Fig. 4(c), right axis), comparable to the volumetric ΔS_M of FeB (–22.4 mJ cm^{-3} K^{-1}). Furthermore, a deviation of the magnetic structure from the previously assumed collinear ferromagnetic ground state may impact the validity of the Σ_M prediction, and the lower than expected magnetocaloric performance is an indicator for more complex magnetic ordering beyond collinear ferromagnetism.

In order to further investigate the coupling of magnetism and crystal structure in this structure, we performed temperature-dependent synchrotron diffraction experiments through the magnetic transition temperature. The unit cell parameters a and c were obtained from sequential Rietveld refinement and indicate spontaneous volume magnetostriction below T_C. The unit cell parameters and unit cell volume show a change in slope at $T_C = 236$ K (Figs. S6 and S7 in the Supplemental Material), indicating spontaneous volume magnetostriction [27, 28] which can be quantified as $\omega = (a - a_p)/a_p$. Here, a is the experimentally observed a (or c) unit cell parameter at a given temperature, and the "paramagnetic" unit cell parameter a_p is approximated by linear extrapolation of the lattice parameter as a function of temperature above the Curie temperature to temperatures below the Curie temperature. The resultant plots of temperature-dependent ω_a and ω_c as compared to $M(T)$ are shown in Fig. 5 In this case, it can clearly be seen that the effect of magnetic ordering near $T_C = 236$ K is to decrease c, indicating negative spontaneous magnetostriction at T_C, while there is negligible magnetostriction in the a direction. There is then another change in slope of the c lattice parameter at $T = 186$, coinciding with and observed kink in the zero-field-cooled $M(T)$, indicating that the magnitude of magnetostructural coupling decreases below this point. Then, at 146 K, coinciding with a kink seen in the field-cooled $M(T)$, the c lattice parameter slope once again increases, and additionally the onset of magnetostriction in the a lattice parameter is observed. From these results, we can clearly see that the observed magnetic transitions in MnPtGa are coupled to changes in the crystal structure.

Overall, the spontaneous volume magnetostriction (Figs. S6 and S7 of the Supplemental Material) is negative in MnPtGa, which is somewhat unusual in Mn-based intermetallics. Often, magnetic ordering leads to expanded volume in such systems, as magnetism favors localization of the itinerant electrons [11, 29–35]. However, in a few cases negative volume magnetostriction has been reported, such as in the antiferromagnets MnO and MnS [36] and the magnetocalorics Mn_5Ge_3 [37] and $Mn_{1+x}Sb$ [38]. In these cases, the volume-dependence of the magnetic exchange energy is implicated as the dominant driver of the magnetostructural interaction. This volume-dependence may in principle be either positive or negative, with a negative dependence indicating that the magnetic exchange energy decreases as the atoms move apart, leading to a negative contribution to the magnetostriction as is often seen in lanthanide-based magnets [39].

C. Magnetic structure

In order to determine the temperature evolution of magnetic structure of MnPtGa, NPD data were collected at various temperatures (Fig. 6) between 300 K and 10 K. At 300 K, only peaks and intensity corresponding to the nuclear Ni_2In ($P6_3/mmc$) structure are observed. At 200 K, below T_C but above the first kink in the temperature-dependent magnetization, additional intensity is observed on some of the low-Q nuclear peaks, but no new peaks arise. This is consistent with a ferromagnetic structure with a moment of approximately $3\,\mu_B$ on each Mn, pointing in the c-direction (Fig. 8(a).

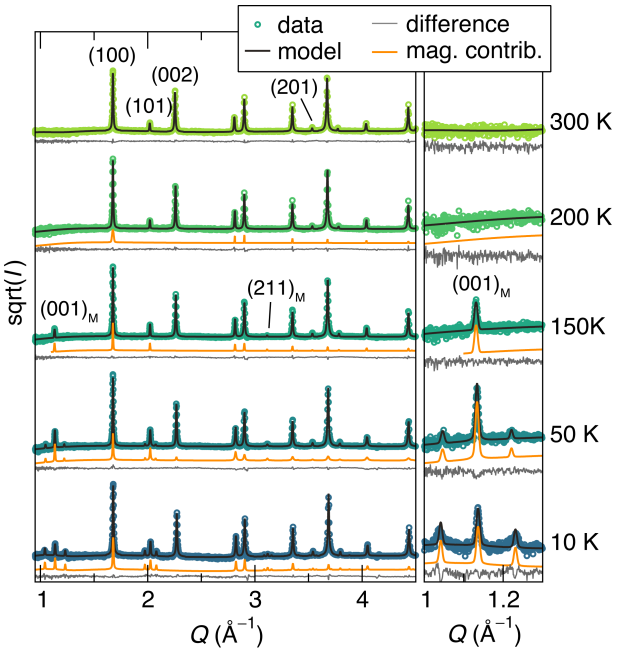

FIG. 6. Magnetic Rietveld refinements of POWGEN data collected using center wavelength 2.665 Å at 300 K, 200 K, 150 K, 50 K, and 10 K. The 300 K pattern contains only nuclear intensity, the 200 K pattern shows the addition of additional magnetic intensity on the nuclear peaks, and the 150 K and below patterns show new principal peaks and magnetic satellites. The right shows a closer view of the (001) magnetic peak and its satellites.

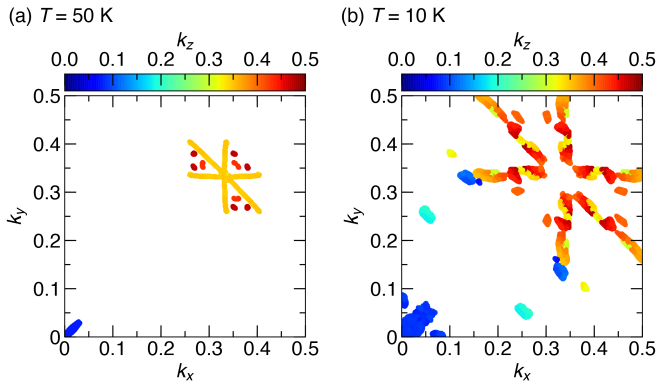

FIG. 7. Space of plausible k-vectors consistent with the two sets of magnetic satellites observed at 50 K (a) and the four sets at 10 K (b). Each possible k-vector with K-SEARCH R Factor less than 0.4 (for 50 K) or 3 (for 10 K) is displayed as a point. These maps reveal that the possible k-vectors at both temperatures cluster in high-symmetry lines and points around (1/3, 1/3, 1/3) and (0, 0, z).

At around 186 K, we see a change in slope in the temperature-dependent magnetization. Below this slope change, at 150 K, additional neutron diffraction peaks are observed [Fig. 6(c)], corresponding to the structurally-forbidden (001) and (211) indexes of the hexagonal nuclear unit cell. Because both of these peaks correspond to an integer index within the primitive nuclear unit cell, we can conclude that the magnetic structure has a k-vector of (0,0,0) (*i.e.* the nuclear and magnetic unit cell are the same). We next used the ISODISTORT software to generate the possible irreducible representations (irreps) and order parameter directions (OPDs) for magnetic structures with moments on the Mn site consistent with this k-vector. We find an excellent fit to the data with the mΓ_5^+ irrep and P_2 OPD, giving the canted magnetic structure shown in Fig. 8(b) with magnetic spacegroup $Cm'c'm$. In this structure, only two magnetic modes are active: one which gives ferromagnetic moment components in the c direction, and one which gives antiferromagnetic moment components pointed in the a direction and alternating direction along the c axis. The resulting structure may be thought of as a canting from the ferromagnetic structure in alternate directions, or as a heavily canted antiferromagnet with moment switching along the c axis. This magnetic structure is similar to that reported for MnPdGa [40] and MnCoSn [41, 42] at low temperatures, although in MnPdGa the antiferromagnetic mode is dominant and the structure is closer to an antiferromagnet. In MnPdGa, the moments are canted 56° from the c axis [40], in MnCoSn they are canted 34(4)° [42], and in MnPtGa they are canted 24(1)°. This structure results in a net ferromagnetic moment of 2.44(6) μ_B along the c axis in MnPtGa.

Near 140 K, we see an additional slope change in the temperature-dependent magnetization. Below this kink, at 50 K, we see satellite peaks emerge in the NPD data about some of the nuclear and magnetic peaks. At 50 K, satellites are visible about the (001) magnetic peak and (101) nuclear/magnetic peak (Fig. 6). At 10 K, these satellites grow stronger and additional satellites about the (211) magnetic peak and (201) nuclear/magnetic peak can be resolved. The satellites indicate the presence of an modulated magnetic structure, with an additional k-vector to the (0,0,0) k-vector identified at 150 K. In order to determine the new magnetic unit cell, we used the program K-SEARCH. This program searches for possible supercells of a given nuclear unit cell that can describe a set of observed satellite positions. Upon searching for commensurate k-vectors, we identified that all but the weakest of the 10 K satellites could be well-fit using a (1/3, 1/3, 1/3) k-vector, indicating a magnetic cell that is tripled along all three hexagonal axes. However, upon enumerating the possible irreps and OPDs consistent with this k-vector, we were unable to satisfactorily fit the peak intensities.

We therefore proceeded to revisit the chosen k-vector, expanding the search to incommensurate vectors. This search, which is equivalent to indexing a powder pattern with an arbitrary triclinic cell, yielded tens of thousands of possible k-vectors spanning different areas of k-space, many with approximately equal R factors (a goodness of fit indicator calculated by summing d-space deviations of the observed satellites from predicted satellite posi-

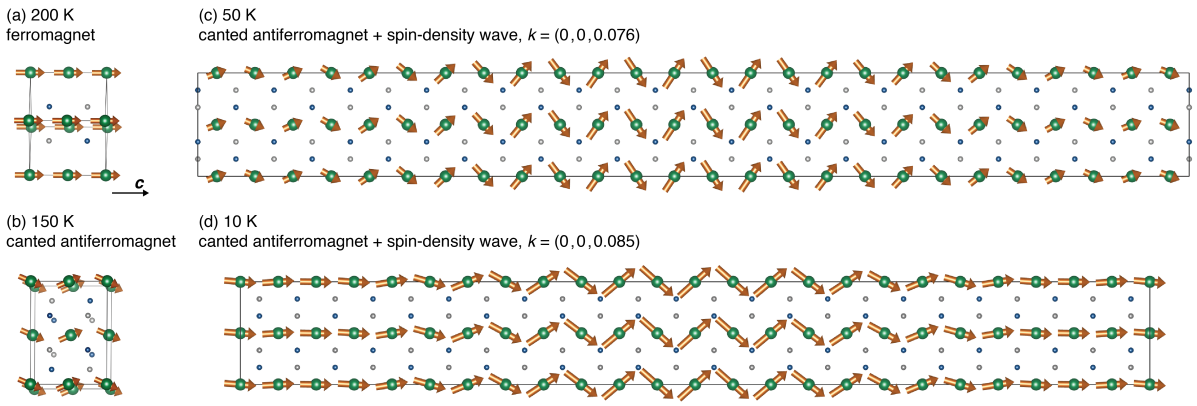

FIG. 8. The evolution of the magnetic structure of MnPtGa from neutron powder diffraction is shown. It transitions from a ferromagnet at 200 K (a) to a canted antiferromagnet at 150 K (b) to a canted antiferromagnet plus spin density wave that increases in amplitude upon cooling to 10 K (c) and (d). For (c) and (d), the unit cells drawn are commensurate unit cells used to approximate the incommensurate magnetic structures.

tions). In order to understand these results, we plotted them in k-space, as shown in 7. We found that at both 10 K and 50 K, plausible k-vectors often clustered around (1/3, 1/3, 1/3) and in high-symmetry lines from this position. However, additional clusters also exist around the (0,0,z) position, with $z = 0.076$ at 50 K and $z = 0.085$ at 10 K. These k-vectors indicate magnetic structures with long-period (approximately 12 or 13 unit cell) incommensurate 1-D modulations along the c axis.

Using the (0,0,z) k-vectors, a simple magnetic structure was obtained that correctly models all satellite positions and intensities in both the 10 K and 50 K pattern [Fig. 8(c)-(d)]. In addition to the $k = (0,0,0)$ modes previously identified, a second irrep becomes active: the incommensurate mΔ_2 irrep with the P OPD. In order to refine the magnetic structure in TOPAS Academic, which does not support refining incommensurate structures, we approximated the periodicity using cells with c-axis set to the integer multiple of the nuclear c axis closest to $1/z$. This corresponds to 13 unit cells at 50 K and 12 unit cells at 10 K. Using these descriptions, only a single new mode (in addition to the two modes refined at 150 K) was needed to describe the patterns at both 50 K and 10 K: an antiferromagnetic spin-density wave with moments oriented in the hexagonal a direction and flipping along the c axis (mΔ_2 $E_g(a)$). This mode modulates the magnitude of the antiferromagnetic component of the magnetic structure in a sine wave with a period of 12 or 13 unit cells, resulting in the fascinating canted spin-density structures depicted in Fig. 8(c)-(d). The magnitude of this mode is relatively small at 50 K, which is why only two sets of satellites were resolvable in the diffraction data. At 10 K, this mode is stronger and four sets may be resolved. At this temperature, the moment on the Mn in the c-direction is 3.1 μ_B, and the moment in the ab-plane oscillates between 3 μ_B and -3 μ_B. The details of crystallographic data refinement are presented in Table I.

It is interesting to ask whether this incommensurate magnetic structure along the c axis also forms in the skyrmion-hosting sample of MnPtGa reported by Srivastava *et al.*, as the skyrmions themselves are incommensurate magnetic structures with very long unit cells modulating in the ab plane (in this case, wavelengths on the order of 800 nm–1800 nm). Most skyrmion hosts that have been studied are assumed to show ferromagnetic ordering within the unit cell, which then rotates over long periods to form the interesting topological magnetic states. However, in some cases more exotic local magnetic structures have been found to interact in interesting ways with long-period skyrmionic order. For example, this occurs in the multiferroic ferrimagnet Cu_2OSeO_3[43], the ferrimagnetic antiskyrmion host $Mn_{1.4}Pt_{0.9}Pd_{0.1}Sn$ [44], compensated ferrimagnetic films of GdCo [45], and in the spin-glass state of $Co_xZn_yMn_z$ [46, 47]. We are not aware of any so-far-reported skyrmion hosts in which the local magnetic structure involves a shorter-period incommensurate spin wave.

We also note that solving magnetic structures from unpolarized powder diffraction data necessarily involves some ambiguity. The solutions we have presented are the highest-symmetry, simplest solutions that we found to satisfactorily reproduce the observed neutron diffraction patterns. However, more complex structures may fit the data equally well. In particular, powder diffraction cannot determine the moment orientation within the hexagonal ab plane. Furthermore, an antiferromagnetic helical mode with constant moment magnitudes rotating in the ab plane with $1/z$ period fits the satellites equivalently to the magnitude-modulated mode we have presented. However, this mode leads to a much lower-symmetry cell, and, furthermore, the constructive and destructive interaction of this mode with the k=0 antiferromagnetic mode causes the overall magnetic structure to show a

TABLE I. Crystallographic Data for MnPtGa

Temperature (K)	10	50	150	200	300
space group (no.)	$C2'/m'$ (12.62)[a]	$Amm'2'$ (38.190)[a]	$Cm'c'm$ (63.462)	$Cm'c'm$ (63.462)	$P6_3/mmc$ (194)
a (Å)	7.4894(3)	72.011(8)	4.3298(4)	4.3308(5)	4.3304(2)
b (Å)	4.3240(1)	4.3281(5)	7.4994(8)	7.5011(8)	/
c (Å)	66.380(4)	7.4966(2)	5.5538(5)	5.5610(1)	5.5726(6)
α, β, γ	90, 90, 90	90, 90, 90	90, 90, 90	90, 90, 90	90, 90, 120
V (Å^3)	2150.4(4)	2336.5(6)	180.33(2)	180.65(3)	90.50(1)
net ferromagnetic moment (μ_B)	3.1(3)	2.0(9)	2.5(6)	3.1(6)	/
local moment magnitude (μ_B)	3.4–4.5	2.2–3.7	2.7	3.1	/
GOF (R_{wp}/R_{exp})	3.341, 2.702[b]	3.989	3.502	2.695	2.629, 2.936[b]

[a] Space groups and lattice parameters provided for 10 K and 50 K are for the commensurate unit cells used to approximate the incommensurate magnetic structure.
[b] GOF for data with center wavelength 2.665 Å and 0.8 Å co-refinement.

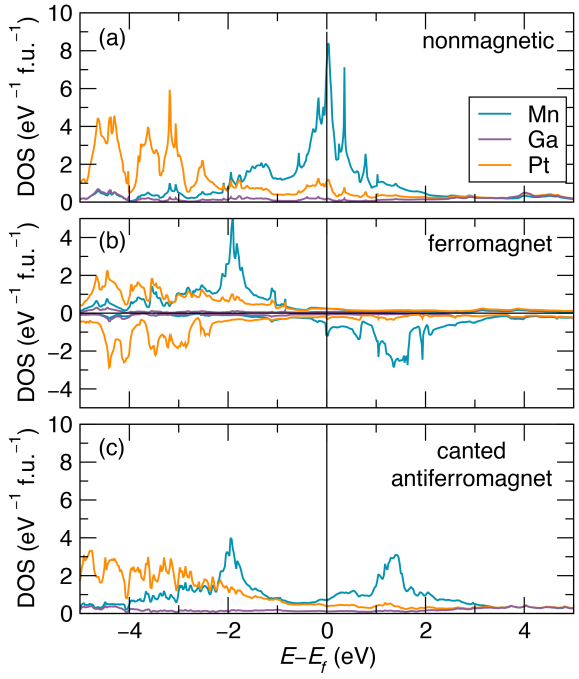

FIG. 9. The site-projected calculated density of states (DOS) diagram are shown in (a) the non–spin polarized state, (b) the spin–polarized state with collinear ferromagnetic order with a small peak in the minority spin channel, and (c) the spin–polarized state with non-collinear magnetic order consistent with the solved magnetic structure.

spin density-wave-like structure in either case. Future studies on single crystal samples of MnPtGa, as well as an examination of the field-driven evolution of magnetic structure, could prove interesting to elucidate complexities of the magnetic and structural phase diagram and establish control over the structure and magnetic properties of this versatile material.

Figure 9 shows the site-projected calculated density of states (DOS) for MnPtGa in (a) the non spin–polarized state, (b) the spin–polarized state with collinear ferromagnetic order (no spin-orbit coupling included) and (c) with spin-orbit coupling in the $k = 0$ structure observed in the neutron diffraction data at 150 K [Fig. 8(b)]. In the non spin–polarized state, the Mn states form a strong peak at the Fermi level, with a total DOS at the Fermi level $N(E_F = 9.27\,\text{eV}^{-1}$ per formula unit. This peak represents an electronic instability which may be relieved by an electronic distortion into a spin-polarized state. The Stoner criterion [$I \cdot N(E_F) > 1$]. For a typical value of the Mn exchange energy (I) of 0.4 eV [48], MnPtGa easily satisfies this criterion.

TABLE II. Results of DFT Calculations on MnPtGa With Different Magnetic Structures

	$E - E_{\min}$ (meV f.u.$^{-1}$)	local moment (μ_B)	net moment (μ_B f.u^{-1})
nonmagnetic	1476		
ferromagnetic[a]	12.9	3.59	3.59
canted[b]	0	3.57	3.30

[a] Moments oriented along hexagonal c axis.
[b] Structure shown in Fig. 8(b).

When a spin-polarized ferromagnetic calculation is performed [Fig. 9(b)], a Mn moment of 3.58 μ_B is found to form, with no substantial moment on the Pt and Ga ions. This spin-polarization greatly reduces the density of states at the Fermi level [Fig. 9(b)]. Interestingly, however, a small peak in the minority spin channel remains. This leads to a total DOS at the Fermi level of 2.46 eV^{-1} per formula unit, which still gives $I \cdot N(E_F) = 0.98$. This peak at the Fermi level is not relieved by the inclusion of spin-orbit coupling in the ferromagnetic calculation and the orientation of the moments in either the [001] or [100] directions Supplemental Material Fig. S8). Therefore, it appears that a ferromagnetic spin structure can stabilize the electronic structure with respect to the nonmagnetic state, but that there is still an opportunity for

subsequent symmetry-lowering magnetic transitions to lower the energy even further. Indeed, when a spin-polarized calculation is performed that is consistent with the canted antiferromagnetic state, the peak at the Fermi level is eliminated [$I \cdot N(E_F) = 0.57$] and the overall energy of the calculation is decreased by. This stabilization explains why MnPtGa transitions from the ferromagnetic to canted antiferromagnetic states as it is cooled below 200 K. We have not, however, attempted calculations on the incommensurate magnetic states we observed at lower temperature in the neutron diffraction.

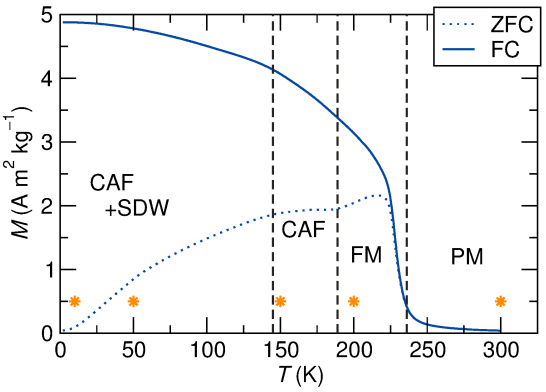

FIG. 10. The proposed phase diagram of MnPtGa from room temperature to 2 K includes a paramagnetic (PM) region to 236 K, collinear ferromagnetism (FM) from 236 K to 175 K, a canted antiferromagnet (CAF) from 175 K to 148 K, and a CAF + spin density wave (SDW) from 148 K to 2 K. The vertical lines indicate kinks in M vs T data and asterisks indicate temperatures at which neutron diffraction data were obtained and analyzed.

III. CONCLUSION

The intermetallic magnet MnPtGa has been prepared and characterized, following the suggestion that it may show strong magnetostructural coupling and a therefore substantial magnetocaloric effects. A small but negative spontaneous volume magnetostriction has been found, associaated with contraction in the interlayer direction upon the onset of magnetic order. The magnetic entropy change associated with the magnetic ordering transition is $-1.99\,\mathrm{J\,kg^{-1}\,K^{-1}}$ for a 5 T applied field. Motovated by the lower-than-expected magnetocaloric effect and anomalies in magnetization measurements, the magnetic structure was examined using neutron powder diffraction and found to evolve as a function of (decreasing) temperature from a ferromagnet, to a canted antiferromagnet, and finally to a canted antiferromagnet with a spin density wave in the c-direction at 10 K (Fig. 10. These deviations from the previously-assumed collinear ferromagnetic structure appear to be in agreement with magnetic measurements, density functional theory calculations, and the measured magnetic entropy change.

ACKNOWLEDGMENTS

This work was supported by the Materials Research Science and Engineering Center (MRSEC) at UC Santa Barbara through NSF DMR-1720256 (IRG-1). The use of the shared facilities of the MRSEC is gratefully acknowledged; the UCSB MRSEC is a member of the Materials Research Facilities Network (www.mrfn.org). J.D.B. acknowledges support from the NSF Graduate Research Fellowship Program under Grant No. 1650114. Use of the Advanced Photon Source at Argonne National Laboratory was supported by the U. S. Department of Energy, Office of Science, Office of Basic Energy Sciences, under Contract No. DE-AC02-06CH11357. A portion of this research conducted at at Oak Ridge National Lab's Spallation Neutron Source, was sponsored by the Scientific User Facilities Division, Office of Basic Energy Sciences, U.S. Department of Energy.

[1] E. P. Wohlfarth, Adv. Phys. **8**, 87 (1959).
[2] P. Kumar, A. Kashyap, B. Balamurugan, J. E. Shield, D. J. Sellmyer, and R. Skomski, J. Physics: Condensed Matter **26**, 064209 (2014).
[3] A. Kussmann and G. Von Rittberg, Zeit. Metallkunde **41**, 470 (1950).
[4] S. Khmelevskyi, I. Turek, and P. Mohn, Phys. Rev. Lett. **91**, 037201 (2003).
[5] L. H. Lewis, C. H. Marrows, and S. Langridge, J. Phys. D: Appl. Phys. **49**, 323002 (2016).
[6] M. G. Vergniory, L. E. annd F. Orlandi, B. Balke, Y.-H. Chan, J. Nuss, A. P. Schnyder, and L. M. Schoop, Eur. Phys. J. B **91**, 213 (2018).
[7] K. H. J. Buschow, Phys. Status Solidi **76**, 615 (1983).
[8] A. K. Srivastava, P. Devi, A. K. Sharma, T. Ma, H. Deniz, H. L. Meyerheim, C. Felser, and S. S. Parkin, Adv. Mater. , 1904327 (2019).
[9] J. D. Bocarsly, E. E. Levin, C. A. C. Garcia, K. Schwennicke, S. D. Wilson, and R. Seshadri, Chem. Mater. **29**, 1613 (2017).
[10] C. A. Garcia, J. D. Bocarsly, and R. Seshadri, Phys. Rev. Mater. **4**, 024402 (2020).
[11] J. D. Bocarsly, E. E. Levin, S. A. Humphrey, T. Faske, W. Donner, S. D. Wilson, and R. Seshadri, Chem. Mater. (2019).
[12] A. Huq, M. Kirkham, P. F. Peterson, J. P. Hodges, P. S. Whitfield, K. Page, T. Hugle, E. B. Iverson, A. Parizzi, and G. Rennich, J. Appl. Crystallogr. **52**, 1189 (2019).
[13] J. Rodríguez-Carvajal, Physica B **192**, 55 (1993).
[14] B. J. Campbell, H. T. Stokes, D. E. Tanner, and D. M.

Hatch, J. Appl. Crystallogr. **39**, 607 (2006).
[15] H. T. Stokes, D. M. Hatch, and B. J. Campbell, ISODISTORT, Isotropy Software Suite, iso.byu.edu.
[16] A. A. Coelho, J. Appl. Crystallogr. **51**, 210 (2018).
[17] K. Momma and F. Izumi, J. Appl. Crystallogr. **44**, 1272 (2011).
[18] B. H. Toby and R. B. Von Dreele, J. Appl. Crystallogr. **46**, 544 (2013).
[19] J. J. Stickel, Comput. Chem. Eng. **34**, 467 (2010).
[20] J. D. Bocarsly, R. F. Need, R. Seshadri, and S. D. Wilson, Phys. Rev. B **97**, 100404 (2018).
[21] G. Kresse and J. Furthmüller, Phys. Rev. B **54**, 11169 (1996).
[22] P. E. Blöchl, Phys. Rev. B **50**, 17953 (1994).
[23] G. Kresse and D. Joubert, Phys. Rev. B **59**, 1758 (1999).
[24] J. P. Perdew, K. Burke, and M. Ernzerhof, Phys. Rev. Lett. **77**, 3865 (1996).
[25] K. H. J. Buschow and D. B. de Mooij, J. Less Common Met. **64**, 1 (2001).
[26] A. Arrott, Phys. Rev. **108**, 1394 (1957).
[27] J. Kusz, S. Juszczyk, and J. Warczewski, J. Appl. Crystallogr. **21**, 898 (1988).
[28] A. Bombik, H. Bohm, J. Kusz, and A. W. Pacyna, J. Magn. Magn. Mater. **234**, 443 (2001).
[29] E. Wohlfarth, Physica B+C **91**, 305 (1977).
[30] T. Moriya and K. Usami, Solid State Commun. **34**, 95 (1980).
[31] M. Shiga, H. Wada, and Y. Nakamura, J. Magn. Magn. Mater. **31-34**, 119 (1983).
[32] V. A. Chernenko, L. Wee, P. G. McCormick, and R. Street, J. Appl. Phys. **85**, 7833 (1999).
[33] A. M. Kadomtseva, Y. F. Popov, G. P. Vorob'ev, K. I. Kamilov, V. Y. Ivanov, A. A. Mukhin, and A. M. Balbashov, Phys. Solid State **42**, 1110 (2000).
[34] R. Huang, Y. Liu, W. Fan, J. Tan, F. Xiao, L. Qian, and L. Li, J. Am. Chem. Soc. **135**, 11469 (2013).
[35] F. Hu, F. Shen, J. Hao, Y. Liu, J. Wang, J. Sun, and B. Shen, Front. Chem. **6**, 1 (2018).
[36] B. Morosin, Phys. Rev. B. **1**, 236 (1970).
[37] H. Ido, T. Suzuki, and T. Kaneko, J. Phys. Soc. Jpn. **29**, 1490 (1970).
[38] J. A. Cooley, M. K. Horton, E. E. Levin, S. H. Lapidus, K. A. Persson, and R. Seshadri, Chem. Mater. **32**, 1243 (2020).
[39] A. Lindbaum and M. Rotter, in *Handbook of Magnetic Materials*, Vol. 14 (2002) pp. 307–362.
[40] H. Shiraishi, T. Hori, N. Ohkubo, K. Ohoyama, and Y. Yamaguchi, J. Appl. Phys. **93**, 6996 (2003).
[41] W. Bażla, A. Szytuła, and W. Zajac, Solid State Commun. **38**, 875 (1981).
[42] H. Shiraishi, T. Hori, N. Ohkubo, and K. Ohoyama, Physica B **384**, 319 (2006).
[43] S. Seki, X. Z. Yu, S. Ishiwata, and Y. Tokura, Science **336**, 198 (2012).
[44] A. K. Nayak, V. Kumar, T. Ma, P. Werner, E. Pippel, R. Sahoo, F. Damay, U. K. Rößler, C. Felser, and S. S. P. Parkin, Nature **548**, 561 (2017).
[45] L. Caretta, F. Büttner, K. Ueda, B. Pfau, C. M. Günther, P. Hessing, A. Churikova, C. Klose, M. Schneider, D. Engel, C. Marcus, D. Bono, K. Bagschik, S. Eisebitt, and G. S. D. Beach, Nat. Nanotechnol. **13**, 1154 (2018).
[46] K. Karube, J. S. White, D. Morikawa, C. D. Dewhurst, R. Cubitt, A. Kikkawa, X. Yu, Y. Tokunaga, T. Arima, H. M. Rønnow, Y. Tokura, and Y. Taguchi, Sci. Adv. **4**, eaar7043 (2018).
[47] J. D. Bocarsly, C. Heikes, C. M. Brown, S. D. Wilson, and R. Seshadri, Phys. Rev. Materials **3**, 014402 (2019).
[48] J. F. Janak, Phys. Rev. B **16**, 255 (1977).

Evolution of non-collinear magnetism in magnetocaloric MnPtGa

Joya A. Cooley,[1,*] Joshua D. Bocarsly,[1,2] Emily C. Schueller,[1,2]
Emily E. Levin,[1,2] Efrain E. Rodriguez,[3] Ashfia Huq,[4]
Saul H. Lapidus,[5] Stephen D. Wilson,[2] and Ram Seshadri[1,2,6]

[1]*Materials Research Laboratory, University of California, Santa Barbara, 93106*
[2]*Materials Department, University of California, Santa Barbara, 93106*
[3]*Department of Chemistry and Biochemistry,*
University of Maryland, College Park, Maryland 20742
[4]*Neutron Scattering Division, Oak Ridge National Laboratory, Oak Ridge, Tennessee 37831*
[5]*X-ray Sciences Division, Argonne National Laboratory, Lemont, Illinois 60439*
[6]*Department of Chemistry and Biochemistry,*
University of California, Santa Barbara, 93106

[*] jacooley@mrl.ucsb.edu

TABLE I. X-ray fluorescence data for MnPtGa from five data points.

	Mn	Pt	Ga
average weight percent	18.55(7)	21.1(1)	60.3(1)
average composition (moles)	1.067(3)	0.978(3)	0.956(5)

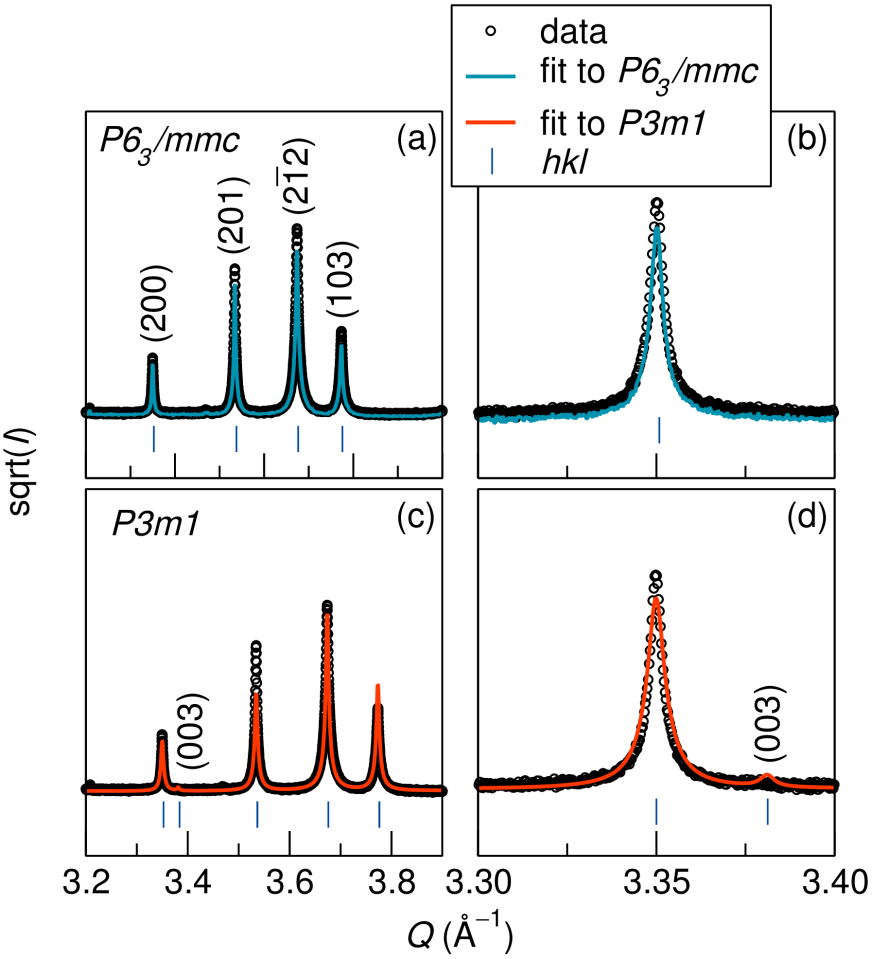

FIG. S1. Room temperature high-resolution synchrotron diffraction data refined in the (a) $P6_3/mmc$ Ni_2In structure and (c) $P3m1$ structure reported by Srivastava *et al* [**?**]. (b) and (d) show zoomed-in portions, showing that the (003) reflection predicted by the $P3m1$ model is not present in the data.

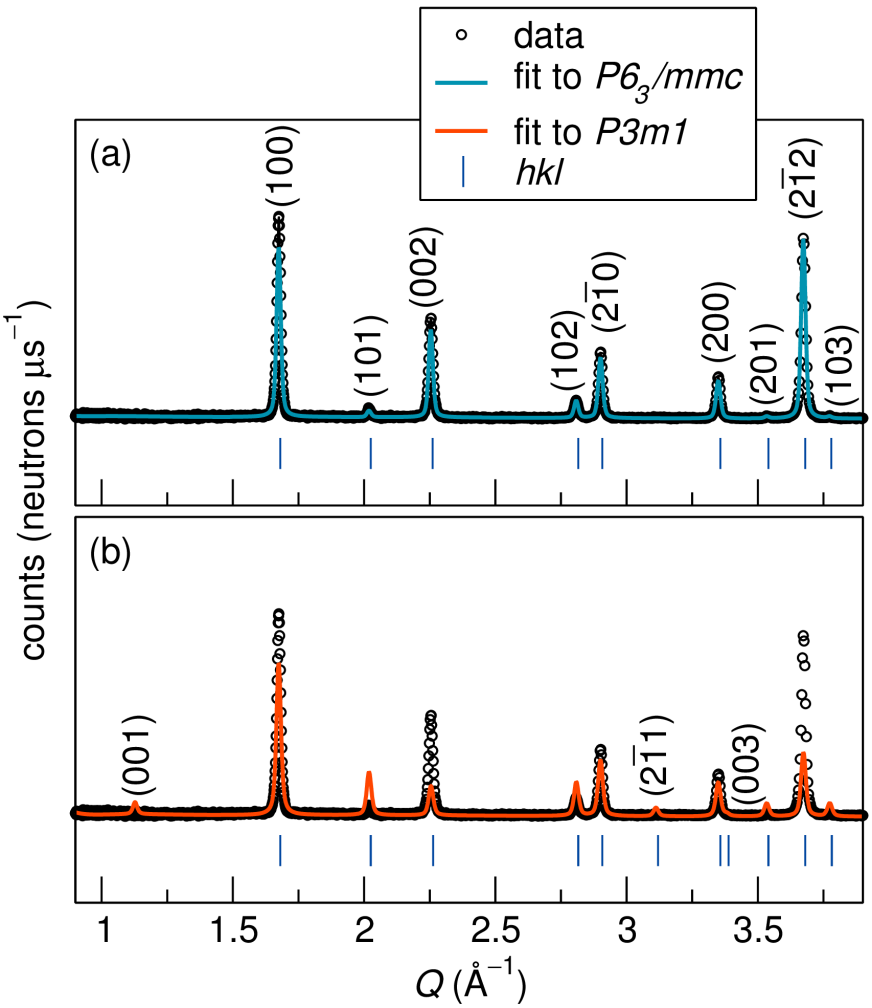

FIG. S2. Room-temperature neutron powder diffraction data refined in the (a) $P6_3/mmc$ Ni_2In and (b) $P3m1$ structure reported by Srivastava *et al.* [**?**]. The latter structural model predicts reflections that are forbidden by $P6_3/mmc$ symmetry and are not observed in the neutron diffraction data.

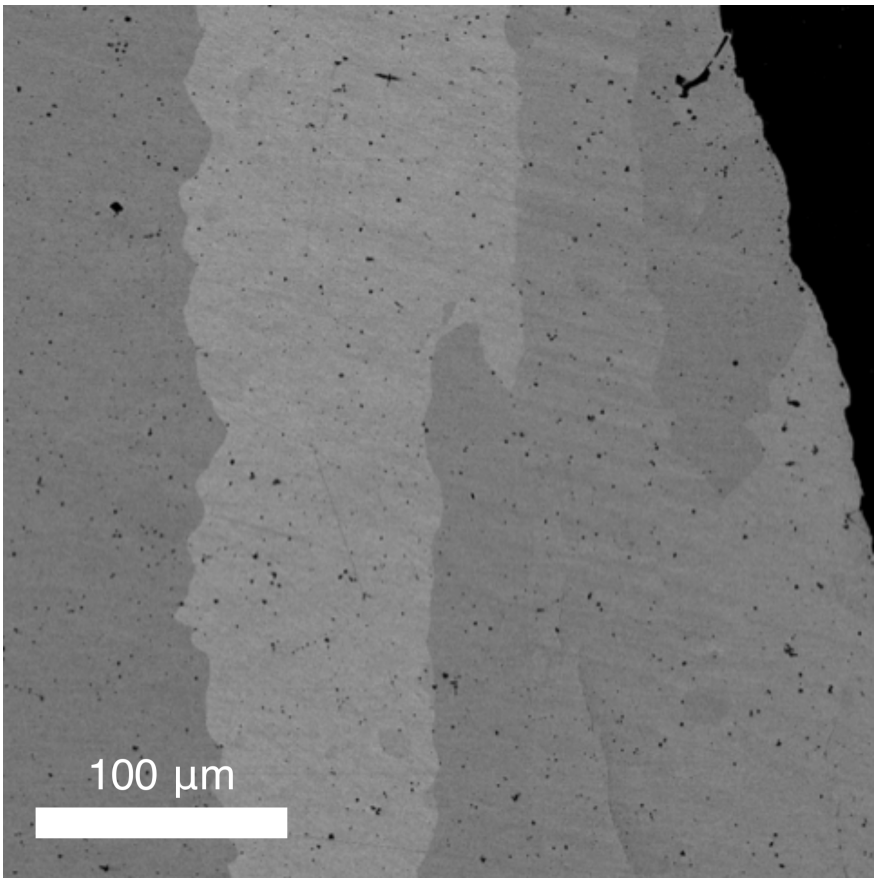

FIG. S3. A backscattered electron microscopy image of the surface of the sample, suggesting compositional uniformity. The observed contrast is due to grain orientation.

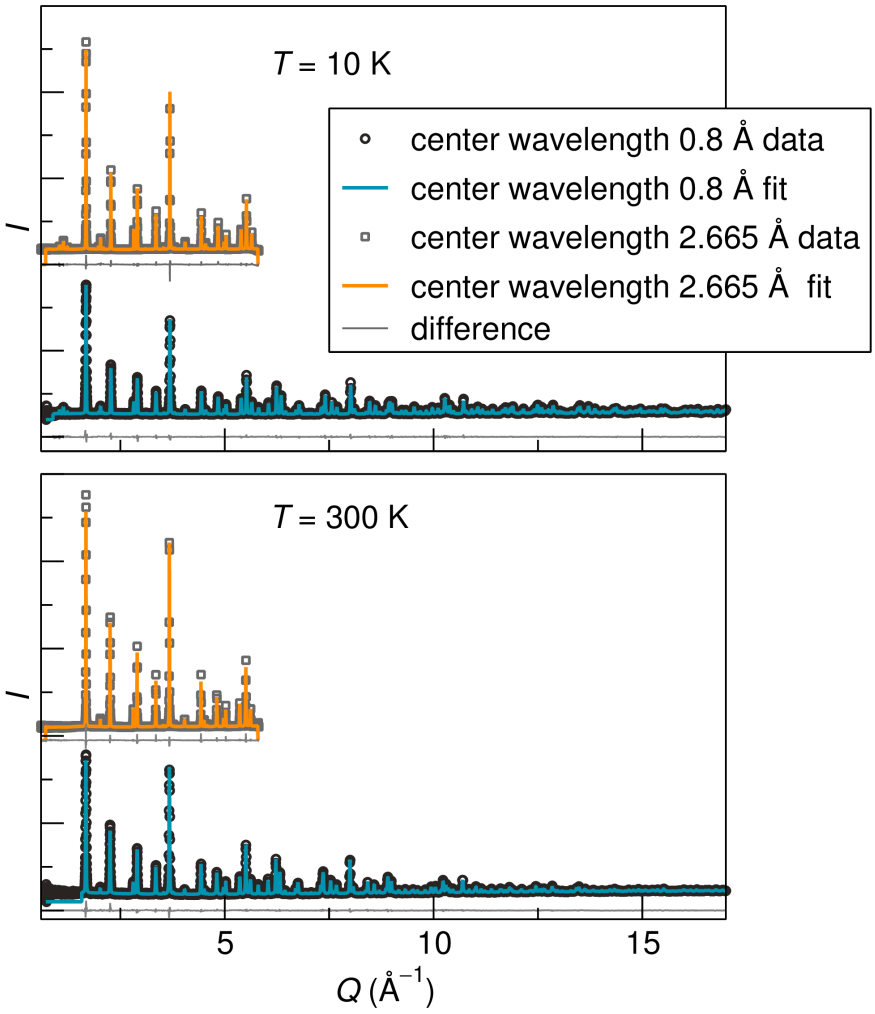

FIG. S4. Rietveld refinement results of neutron powder diffraction data from POWGEN fit to the $P6_3/mmc$ space group are shown at (a) 10 K and (b) 100 K. Data collected with center wavelength 0.8 Å provide a large Q-space range of data and is suitable for refinement of atomic displacement parameters. Data collected with center wavelength 2.665 Å allow for high resolution at low Q, where peaks from magnetic diffraction are present.

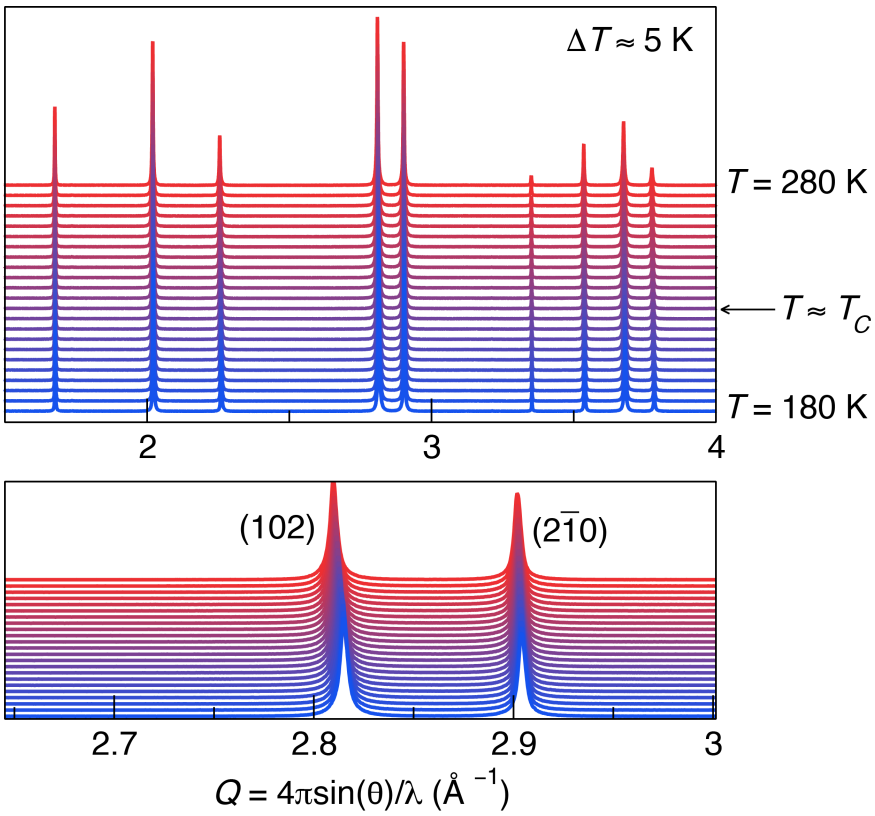

FIG. S5. (a) Temperature-dependent synchrotron X-ray diffraction patterns between 180 K and 280 K are shown. The approximate T_C is indicated. (b) A closer view of the (102) and (2$\bar{1}$0) peaks reveals no new peaks below T_C indicating that the nuclear space group does not change in this temperature range.

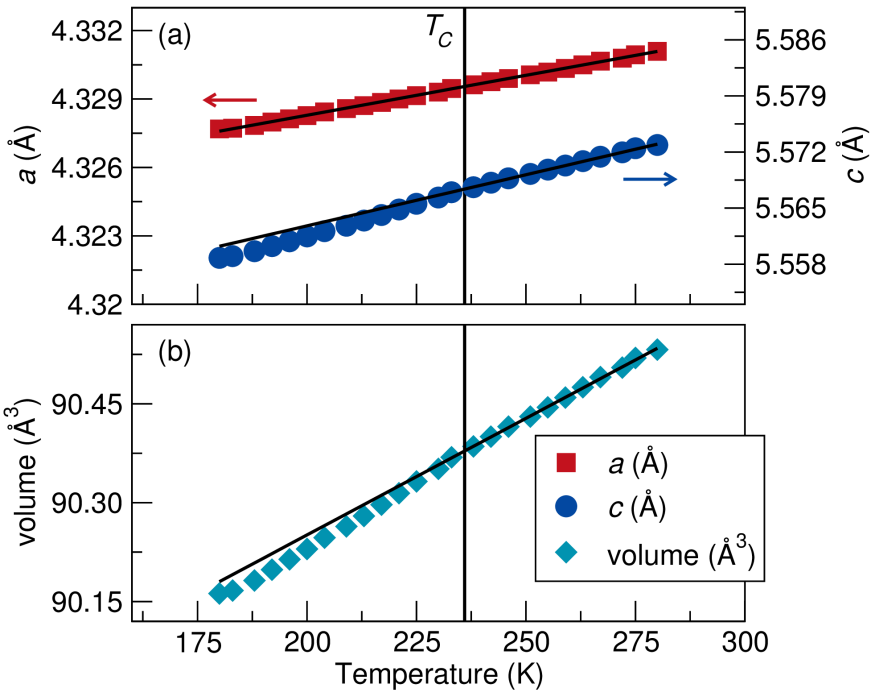

FIG. S6. (a) The temperature-dependence of the a and c unit cell parameters and (b) the unit cell volume of MnPtGa obtained from refinements of synchrotron X-ray data on a point detector between 180 K and 280 K sweeping at a rate of 0.4 K min^{-1}. The solid vertical line indicates the T_C determined using from the Arrott plot. In both panels, the best linear fit to paramagnetic (*i.e.* above T_C) cell parameters and volume are extrapolated below T_C to emphasize the changing thermal expansion coefficients.

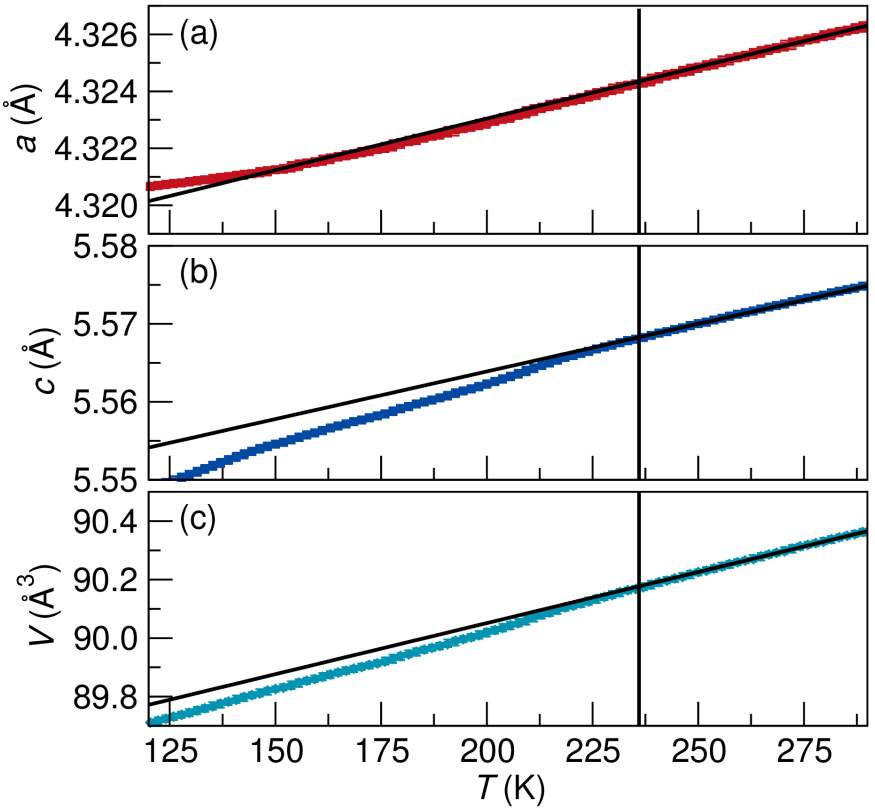

FIG. S7. (a) The temperature-dependence of the a and c unit cell parameters and (b) the unit cell volume of MnPtGa obtained from refinements of synchrotron X-ray data on an area detector between 100 K and 300 K sweeping at a rate of 5 K min^{-1}. The solid vertical line indicates the T_C determined from the Arrott plot. In both panels, the best linear fit to paramagnetic (*i.e.* above T_C) cell parameters and volume are extrapolated below T_C to emphasize the changing thermal expansion coefficients.

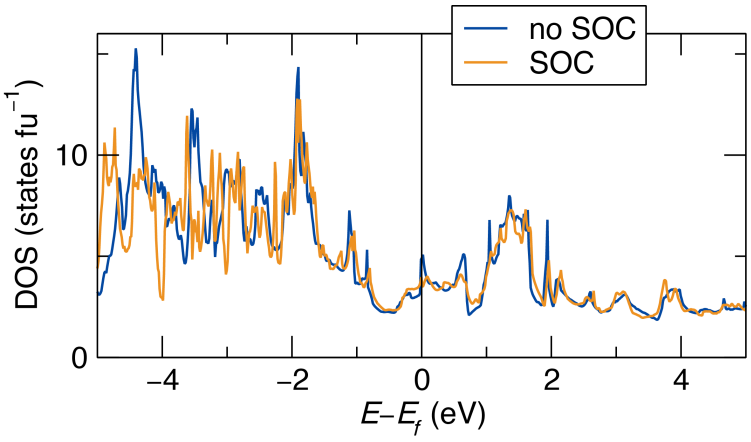

FIG. S8. Comparison of the calculated densities of states with and without spin-orbit coupling for MnPtGa, assuming a collinear ferromagnetic spin structure. For the spin-orbit coupling calculations, the calculation with ferromagnetic moments oriented in the [001] direction is shown. With spin-orbit coupling, the majority and minority spin states are not defined, so all of the electron density is shown in one channel. For the calculation with no spin-orbit coupling, the minority and majority spin channels are added together to allow direct comparison. The densities of states are qualitatively similar near the Fermi level and deviate below the Fermi level.